

# Three-Dimensional Manganese Oxide@Carbon Networks as Free-Standing, High-Loading Cathodes for High-Performance Zinc-Ion Batteries

Xuan Gao, Chengyi Zhang, Yuhang Dai, Siyu Zhao, Xueying Hu, Fangjia Zhao, Wei Zhang, Ruwei Chen, Wei Zong, Zijuan Du, Haobo Dong, Yiyang Liu, Hongzhen He, Jianwei Li, Ivan P. Parkin, Guanjie He,\* and Claire J. Carmalt\*

Zinc-ion batteries (ZIBs), which are inexpensive and environmentally friendly, have a lot of potential for use in grid-scale energy storage systems, but their use is constrained by the availability of suitable cathode materials. MnO<sub>2</sub>-based cathodes are emerging as a promising contenders, due to the great availability and safety, as well as the device's stable output voltage platform (1.5 V). Improving the slow kinetics of MnO<sub>2</sub>-based cathodes caused by low electrical conductivity and mass diffusion rate is a challenge for their future use in next-generation rapid charging devices. Herein, the aforementioned challenges are overcome by proposing a sodium-intercalated manganese oxide (NMO) with 3D varying thickness carbon nanotubes (VTCNTs) networks as appropriate free-standing, binder-free cathodes (NMO/VTCNTs) without any heat treatment. A network construction strategy based on CNTs of different diameters is proposed for the first time to provide high specific capacity while achieving high mass loading. The specific capacity of as-prepared cathodes is significantly increased. The resulting free-standing binder-free cathodes achieve excellent capacity (329 mAh g<sup>-1</sup> after 120 cycles at 0.2 A g<sup>-1</sup> and 225 mAh g<sup>-1</sup> after 200 cycles at 1 A g<sup>-1</sup>) and long-term cycling stability (158 mAh g<sup>-1</sup> at 2 A g<sup>-1</sup> after 1000 cycles).

## 1. Introduction

Aqueous batteries with neutral or weak acidic electrolytes have demonstrated high potential in future energy-storage technologies due to their low cost, high safety, and environmental friendliness.<sup>[1]</sup> As one of the promising aqueous energy-storage technologies, aqueous zinc-ion batteries (ZIBs) provide significant benefits owing to their plentiful resource reserves and volumetric energy density of 5855 mAh cm<sup>-3</sup>, which is higher than that of lithium-ion batteries (2061 mAh cm<sup>-3</sup>).<sup>[2]</sup> Considering the strong electrostatic interaction between Zn<sup>2+</sup> and the crystal structure of the host materials, the development of appropriate cathode materials is an important challenge. Several suitable cathodes for aqueous ZIBs have been developed, including manganese oxides, vanadium oxides, and the Prussian blue analogues (PBAs).<sup>[3]</sup> Compared to the low capacity of the PBA

family and the high cost of vanadium oxides, manganese oxides seem to have more favorable industrialization possibilities.

Manganese oxide-based ZIBs are emerging as a promising contender, due to the abundance, low cost, and safety of raw materials, as well as the output voltage plateaus of ZIBs (1.5 V vs. Zn/Zn<sup>2+</sup>).<sup>[4]</sup> Additionally, numerous charge transport pathways and rich redox reactions of cathodes offer high capacity and excellent energy density. Atomic structures of various manganese oxides, for example,  $\alpha$ -(2 × 2 tunnel),  $\beta$ -(1 × 1 tunnel),  $\gamma$ -(1 × 2 and 1 × 1 tunnel),  $\lambda$ -(spinel type), and  $\delta$ -(layered structure), have been shown to be suitable for ZIBs.<sup>[5]</sup> Although, the tunnel-like structure provides open pathways and abundant active sites for Zn<sup>2+</sup> diffusion and storage, it is always limited by severe structural collapse during the discharge process. Compared with other crystalline polymorphs, layered  $\delta$ -MnO<sub>2</sub> possesses larger spacing channels ( $\approx 70$  Å), which is more favorable for fast and reversible Zn intercalation-extraction.<sup>[6]</sup> However, according to previous detailed studies, the phase transition of layered structure  $\delta$ -MnO<sub>2</sub> during cycling can lead to large volume changes and structural collapse, which seriously affects the cycling stability.<sup>[7]</sup> The cation pre-intercalation is a

X. Gao, Y. Dai, S. Zhao, X. Hu, F. Zhao, W. Zhang, R. Chen, W. Zong, Z. Du, H. Dong, Y. Liu, H. He, J. Li, I. P. Parkin, G. He, C. J. Carmalt  
Christopher Ingold Laboratory  
Department of Chemistry  
University College London  
20 Gordon Street, London WC1H 0AJ, UK  
E-mail: g.he@ucl.ac.uk; c.j.carmalt@ucl.ac.uk

C. Zhang  
Institute of Technological Sciences  
Wuhan University  
Wuhan, Hubei 430072, P. R. China

 The ORCID identification number(s) for the author(s) of this article can be found under <https://doi.org/10.1002/ssr.202200316>.

© 2022 The Authors. Small Structures published by Wiley-VCH GmbH. This is an open access article under the terms of the Creative Commons Attribution License, which permits use, distribution and reproduction in any medium, provided the original work is properly cited.

DOI: 10.1002/ssr.202200316

feasible strategy to achieve stable  $\text{Zn}^{2+}$  storage, among which  $\text{H}^+$ ,  $\text{Li}^+$ ,  $\text{Na}^+$ ,  $\text{K}^+$ ,  $\text{Zn}^{2+}$ ,  $\text{Cu}^{2+}$ , etc., have been applied in previous studies.<sup>[6,8]</sup>

Improving the rate performance of manganese oxide-based cathodes caused by low electrical conductivity ( $10^{-5}$ – $10^{-6}$  S  $\text{cm}^{-1}$ ) and mass diffusion rate is another challenge for their future use in next-generation fast-charging devices.<sup>[9]</sup> To overcome this problem, techniques such as inducing oxygen vacancy or surface carbon coating have been suggested to promote the ionic and electronic transfer within manganese oxide cathodes. However, these methods inevitably introduce high-temperature treatments such as sintering, which is unfavorable for industrialization, and will cause high energy consumption and increase safety hazards in the mass production process. Carbon materials, such as carbon nanotubes (CNTs), graphene, and nitrogen-doped carbon, have excellent electrical conductivity and considerable specific surface area, which can promote electron transport and prevent the agglomeration of active materials.<sup>[10]</sup> Although hybrid materials such as  $\text{MnO}_2/\text{CNTs}$ ,  $\text{MnO}_2/\text{graphene}$ , etc., have been developed, most of the reported cathodes were prepared by traditional slurry coating methods. During the battery manufacturing process, poly(vinylidene fluoride) (PVDF) is often inevitably used during the preparation of ZIBs cathodes. The presence of the polymer binder severely hinders the transport of  $\text{Zn}^{2+}$  at the current collector/active material interface.<sup>[11]</sup> It is well known that the diameter of  $\text{Zn}^{2+}$  is close to that of  $\text{Li}^+$ , which results in a much higher charge density of  $\text{Zn}^{2+}$  than that of  $\text{Li}^+$ , resulting in larger polarization effects during diffusion/transportation.<sup>[12]</sup> Therefore,  $\text{Zn}^{2+}$  tends to adsorb on the C–F bonds in polarized PVDF. As a result, the mobility of  $\text{Zn}^{2+}$  is significantly reduced, resulting in limited rate capacity, cycling stability, and energy density of assembled ZIBs. In this regard, fabricating binder-free electrodes presents an urgent need to avoid the sluggish zinc transport kinetics in polymer binders and extra mass with low utilization rate of active materials.

Herein, we overcome the aforementioned challenges by proposing a sodium-intercalated manganese oxide (NMO) with 3D varying thinness carbon nanotubes (VTCNTs) networks as an appropriate free-standing, binder-free cathode (NMO/VTCNTs) without any heat-treatment. A network construction strategy based on two CNTs of different diameters is proposed for the first time to provide high mass specific capacity while achieving high mass loading. Low-thinness CNTs (LTCNTs, with a diameter of 5–10 nm) and high-thinness CNTs (HTCNTs, with a diameter of 110–150 nm) are used in the process of material synthesis and electrode fabrication to improve specific capacity, electrode flatness, and areal mass loading. The densely interconnected CNT networks in a 3D design can withstand significant deformation while forming interface with NMO to offer extra  $\text{Zn}^{2+}$  storage, facile channels for electrolyte immersing, and efficient transfer routes for  $\text{Zn}^{2+}$ /electron migration. The sheet-like  $\text{Na}_{0.55}\text{Mn}_2\text{O}_4 \cdot 1.5\text{H}_2\text{O}$  is evenly distributed and immobilized in CNTs, increasing its structural stability as well as ion and electron transport rates simultaneously. The prepared free-standing binder-free cathodes are able to achieve a loading of about 5 mg  $\text{cm}^{-2}$  while maintaining excellent electrochemical performance and provide high specific capacities of 329 mAh  $\text{g}^{-1}$  after 120 cycles at a current density of 0.2 A  $\text{g}^{-1}$ , 225 mAh  $\text{g}^{-1}$  after

200 cycles at a current density of 1 A  $\text{g}^{-1}$ , and 158 mAh  $\text{g}^{-1}$  after 1000 cycles at a current density of 2 A  $\text{g}^{-1}$ . As for the electrode preparation process, while maintaining a sufficient material interface between the LTCNTs and the NMO, the HTCNTs were able to increase the loading of active materials to maintain the flatness of the electrode, resulting in a free-standing, binder-free cathodes. This construction strategy of CNT networks with different diameters has a good remark for realizing high mass loading and high capacity and provides an important reference for industrial attempts.

## 2. Results and Discussion

The schematic diagram of the synthesis method of NMO/LTCNTs is shown in **Figure 1a** and is introduced in detail in Experimental Section. The morphology of the synthesized NMO/LTCNTs was confirmed by scanning electron microscope (SEM) and transmission electron microscope (TEM). As shown in **Figure 1b** by SEM, LTCNTs were introduced into sheet-like NMO and exhibits a uniform hybrid structure. The sheet-like NMO exhibits a diameter of 80–300 nm. TEM in **Figure 1c** further shows the NMO exhibits a sheet-like overlapping morphology with CNTs of  $\approx 5$  nm in diameter interspersed. Meanwhile, **Figure 1d** shows LTCNTs with a diameter of  $\approx 5$  nm intercalated between sheet-like NMOs. The sheet-like NMO presents an extremely thin morphology and is in the network of LTCNTs. LTCNTs with a diameter of about 5 nm were able to intercalate between the flake layers of NMO. **Figure 1e** shows the energy dispersive spectrometry (EDS) mapping diagram, which is used to observe the distribution of each element, while **Figures 1f–i** show the specific distribution of Mn, O, Na, and C elements, respectively. It can be seen that the sodium ions show a uniform distribution, and CNTs are also uniformly distributed in the structures.

As shown in **Figure 2a**, free-standing and binder-free NMO/VTCNTs cathodes were obtained by suction filtration. The presence of HTCNTs provides a mechanical support for the electrode and ensures less shrinkage of the cathode during drying. The NMO/VTCNTs used for electrochemical testing were cut into small discs with a diameter of 1.2 cm and an area of about 1.13  $\text{cm}^2$ . As shown in the digital image of **Figure 2b**, the NMO/VTCNTs electrode obtained after suction filtration presents an extremely flat and uniform surface, which is beneficial to the reaction efficiency and electrical conductivity of the interface between the electrolyte and the cathode. Moreover, the inset in **Figure 2b** indicates that the obtained NMO/VTCNTs electrodes exhibit considerable flexibility and can be bent. The wettability to the electrolyte was evaluated first, as shown in **Figure S1a** and **b**, Supporting Information. Due to the porous network provided by CNTs, the wettability of the free-standing binder-free cathode for aqueous 2 M  $\text{ZnSO}_4$  electrolyte is significantly improved compared with the cathode coated on carbon paper. The macroscopic 3D morphology of the fabricated NMO/VTCNTs electrode was examined using X-Ray micro-computed tomography (CT), which depicts a distribution of sheet-like NMO supported on CNT network in 3D space (as shown in **Figure 2c**). After extracting the active material (NMO) phase and pore phase according to the gray scale level using

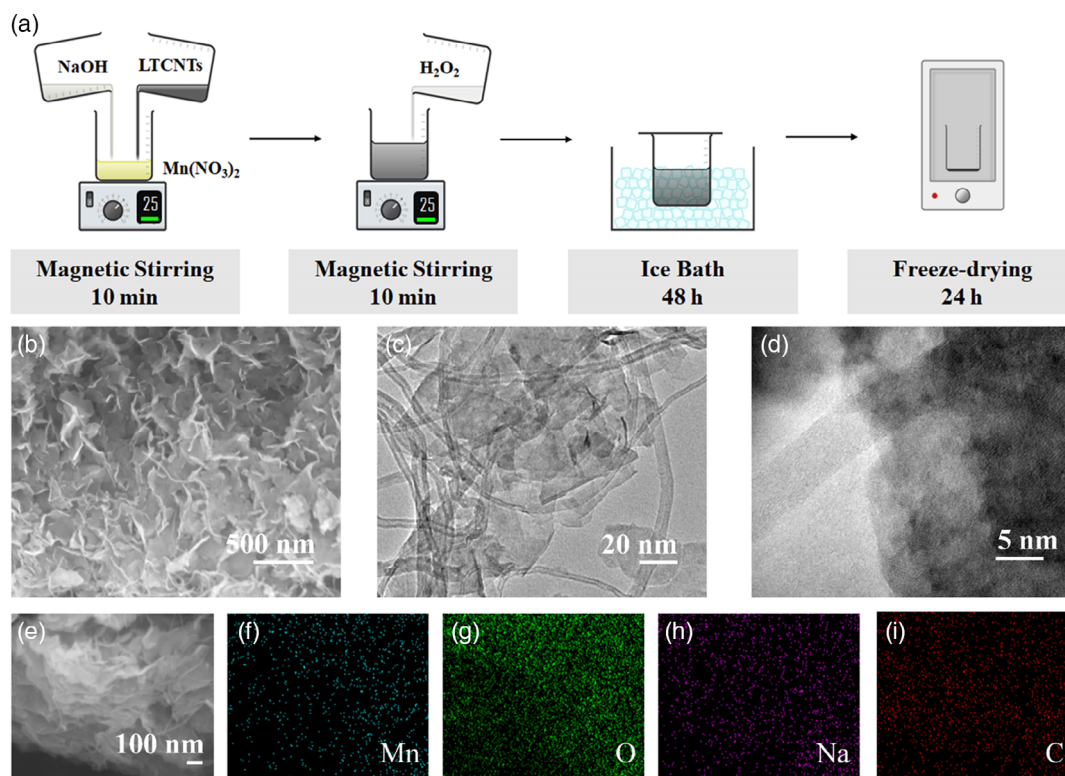


**Figure 1.** a) Schematic diagram of the synthesis method of sodium-intercalated manganese oxide (NMO)/LTCNTs. b) Scanning electron microscope (SEM) and c) transmission electron microscope (TEM) of NMO/LTCNTs. d) Higher-resolution TEM of NMO/LTCNTs clearly shows LTCNTs intercalated in the interlayer of sheet-like NMOs. e, f) EDS mapping images of NMO/LTCNTs shows that NMO and LTCNTs are uniformly distributed.

thresholding segmentation, the skeleton of the active materials can be visualized, from which a complex 3D structure and broad distribution of the pore size were observed. The uniform distribution of CNTs forms network, which provides mechanical support for active material, and makes the prepared NMO/VTCNTs a free-standing electrode. X-Ray diffraction (XRD) patterns of NMO/VTCNTs and pure NMO are first compared in Figure 2d. Due to the introduction of CNTs, the X-Ray scattering is increased, and the peak intensity is weakened.<sup>[13]</sup> However, it is worth noting that the primary hybrid structure of the NMOs and CNTs does not affect the peak positions. The pattern exhibited in Figure 2d coincides well with Birnessite  $\text{Na}_{0.55}\text{Mn}_2\text{O}_4 \cdot 1.5\text{H}_2\text{O}$  (JCPDS no. 43-1456), where  $a = 5.175(3) \text{ \AA}$ ,  $b = 2.849(1) \text{ \AA}$ ,  $c = 7.338(5) \text{ \AA}$ ,  $\alpha = \gamma = 90^\circ$  and  $\beta = 103.19(4)^\circ$ , and  $V = 105.3(6) \text{ \AA}^3$ .<sup>[14]</sup>

X-Ray photoelectron spectroscopy (XPS) was utilized to investigate the atomic ratio and average oxidation state (AOS) of each element on the surface of the material. The relatively high content of O element is due to the surface oxygen absorption. Na was observed as shown in Figure 2f (Na 1s) with a characteristic peak at 1071 eV. Mn 2p has two separate peaks with a binding energy difference of 11.7 eV, whereas the difference is 4.90 eV for the Mn 3s spectrum. Based on the binding energy difference of the Mn 3s peak, the AOS of Mn was calculated to be 3.44 according to the formula  $\text{AOS} = 8.956 - 1.126\Delta\text{Es}$ , where the Mn valence state is close to the value deduced from the elemental composition.<sup>[14]</sup> In terms of O 1s (Figure 2i), the spectrum was convoluted from three corresponding peaks which are

assigned to adsorbed water H–O–H (532.5 eV), surface-adsorbed oxygen ions Mn–OH (531.2 eV), and lattice oxygen species Mn–O–Mn (529.6 eV), respectively.<sup>[15]</sup>

Coin cells (CR2032-type) were assembled to investigate the electrochemical performances of NMO with and without CNTs, while metallic Zn was used as the anodes, which is common in ZIBs research.<sup>[16]</sup> Pure NMO was also synthesized as control materials. Cyclic voltammogram (CV) curves of the NMO/LTCNTs and NMO cathodes with the same fabrication method (with binder and carbon paper collector) were measured at different scan rates of 0.1, 0.2, 0.3, 0.4, 0.5, and  $1 \text{ mV s}^{-1}$  in the potential window of 0.8–1.9 V, respectively, to discuss the effect of LTCNTs on the electrochemical behavior of NMO (as shown in Figure 3a,d). When the scan rate is low, two pairs of reduction and oxidation peaks were observed, with reduction peaks at 1.32 and 1.18 V and oxidation peaks at 1.57 and 1.62 V. The coin cell with the NMO/LTCNTs cathode exhibits a similar redox peak position to that of NMO, indicating the similarity of the two charge storage mechanisms, which shows redox reactions of typical manganese oxide-based cathodes in an aqueous zinc salt ( $\text{ZnSO}_4$ ) electrolyte during cycling.<sup>[17]</sup> As shown in Figure 3d, the two pairs of redox peaks of the NMO electrode without CNTs start to overlap into a single pair from the scan rate of  $0.3 \text{ mV s}^{-1}$ . When the scan rate reaches  $1 \text{ mV s}^{-1}$ , the two oxidation peaks merge into one and shift to a higher voltage. The oxidation peak of the coin cell with NMO cathode under the scan rate of  $1 \text{ mV s}^{-1}$  is 1.66 V, and is shifted by nearly 0.2 V

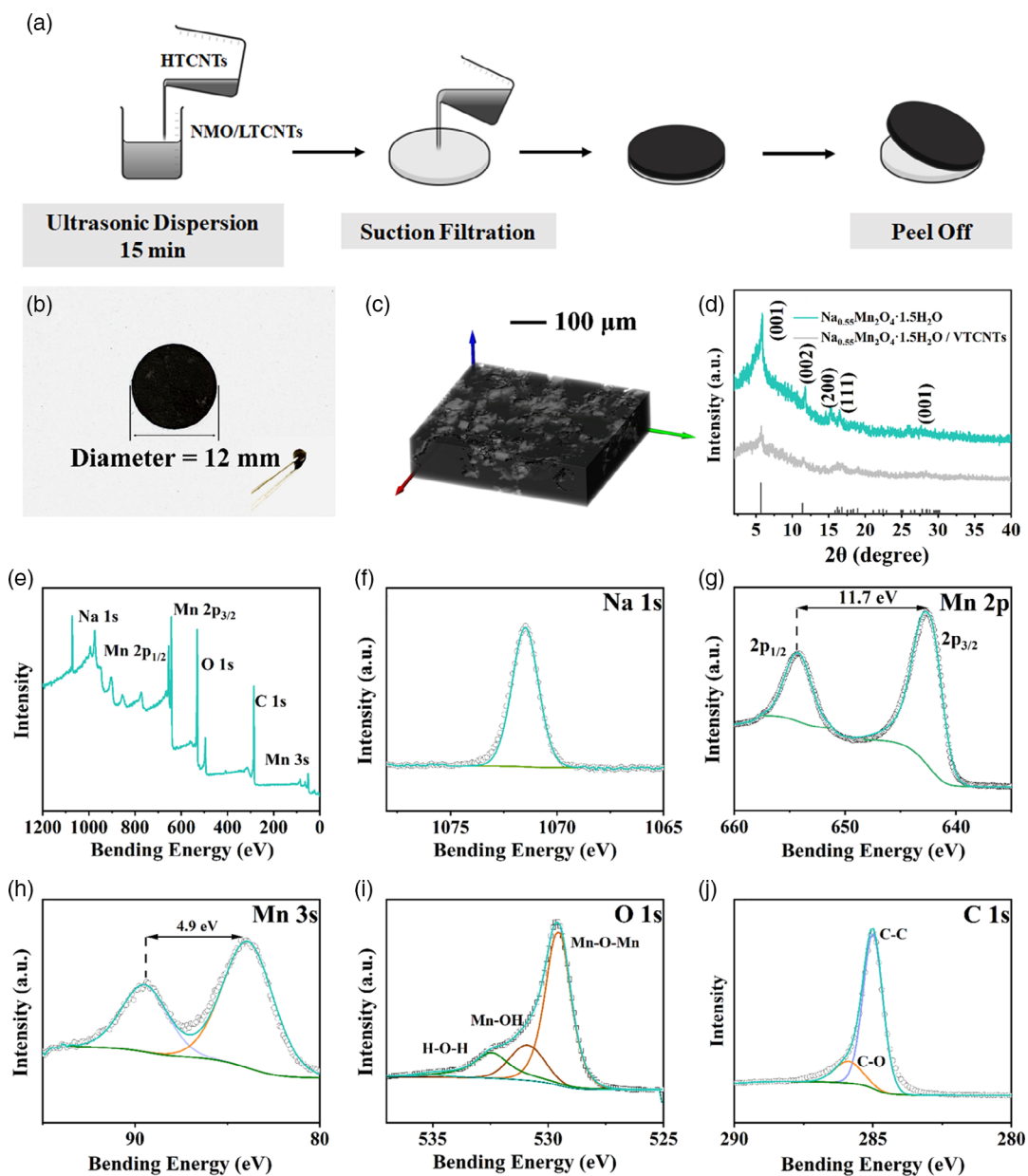


**Figure 2.** a) Schematic diagram of the preparation of free-standing binder-free NMO/VT CNTs cathodes. b) Optical photo of free-standing, binder-free NMO/VT CNTs cathodes, with insets showing that the cathode is flexible and bendable. c) The computed tomography (CT) image of NMO/VT CNTs cathode shows a uniform distribution of active material in the electrode and the supporting role of carbon nanotubes (CNT). d) X-Ray diffraction (XRD) patterns of NMO/VT CNTs and NMO. e) X-Ray photoelectron spectroscopy (XPS) pattern of NMO/VT CNTs with a focus on f) Na 1s, g) Mn 2p, h) Mn 3s, i) O 1s, and j) C 1s.

compared to the case of  $0.1 \text{ mV s}^{-1}$ . The NMO/LTCNTs cathodes exhibit very similar CV curves at different scan rates, which shows that their reaction behaviors and kinetics are similar at high and low rates. Notably, with the increase of scan rates, the height of redox peaks of NMO/LTCNTs cathodes were significantly larger than that of NMO cathodes, showing better conductivity and reaction activity in high scan rates. In general, the potential difference  $\Delta\varphi$  between the oxidation peak and the reduction peak of the quasi-reversible electrochemical reaction gradually increases with the increase of the scan rate.<sup>[18]</sup>

However, for a well-reversible electrochemical system, this situation will be alleviated.<sup>[19]</sup> In Figure 3d, as the scan rate increases, the shifts of P2 and P4 are 0.059 and 0.048 V, respectively. In contrast, the shifts of P1, P2, P3, and P4 of NMO/VT CNT in Figure 3a are only 0.026, 0.021, 0.030, and 0.025 V, respectively, which indicates a more reversible electrochemical system formed by NMO/VT CNTs cathode.

To further investigate the kinetic processes of different cathode materials, their diffusion-controlled and capacitive contributions were evaluated based on the 4 peaks in Figure 3a and

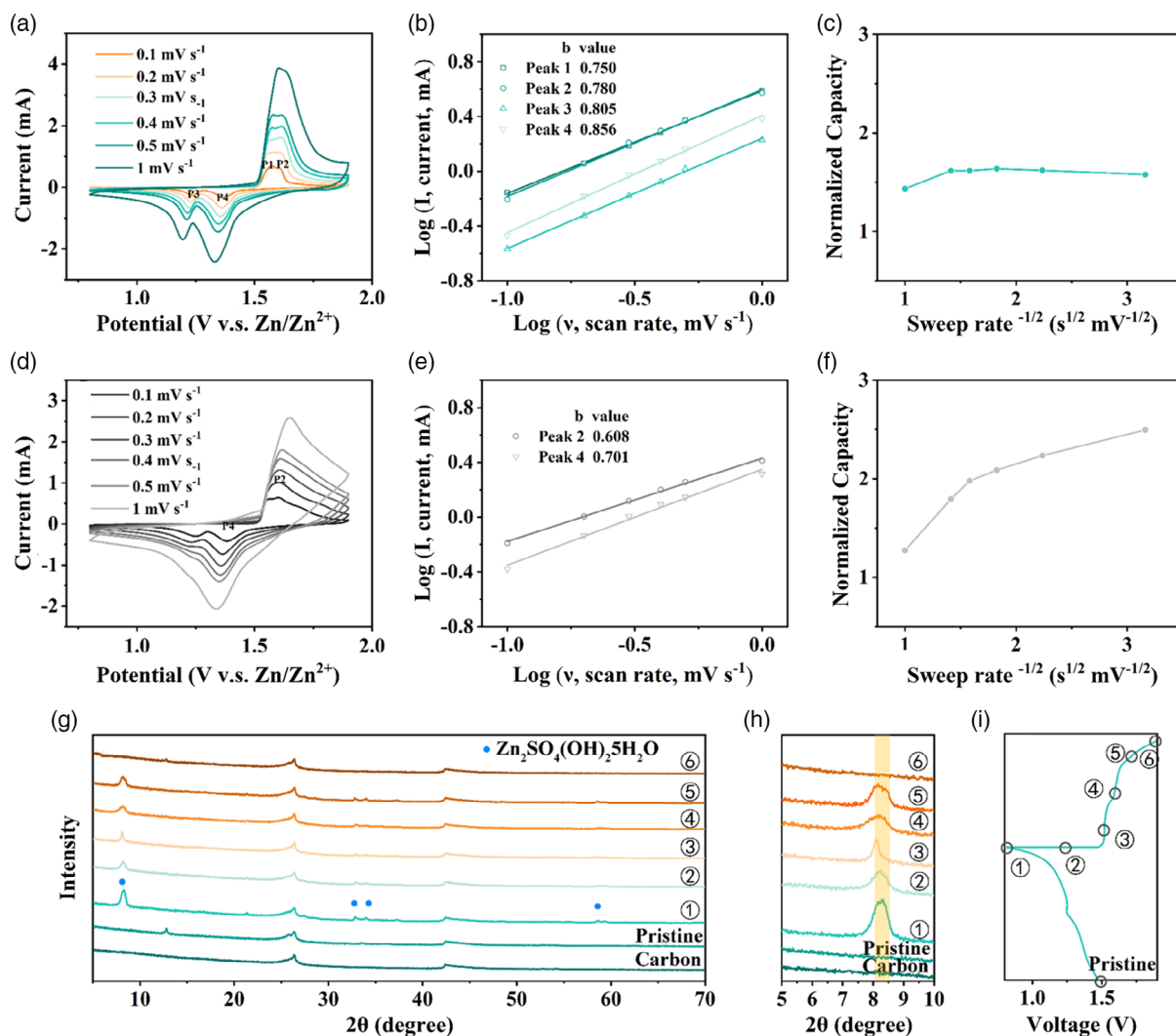


**Figure 3.** a,d) Cyclic voltammogram (CV) curves with scan rates ranging from 0.1 to 1  $\text{mV s}^{-1}$ , b,e) diffusion-capacitive control contribution presented in the bar chart, and c,f) the relationship between normalized capacity and sweep rate of NMO/VTCNTs and NMO, respectively. g) Ex situ XRD spectra for the NMO/VTCNTs cathode in the full cell with h) amplified plots for peak (001) at different states which match with the point marked in i) during the process of charge and discharge.

the 2 peaks in Figure 3d. Theoretically, the peak current ( $i$ ) and sweep rate ( $\nu$ ) should follow the Equation (1)

$$i = a\nu^b \quad (1)$$

hence,  $\log(i) = \log(a) + b \cdot \log(\nu)$ ,

where  $a$  and  $b$  can be calculated by fitting a linear curve to the log-log plot of the peak current and the sweep rates (Figure 3b,e).<sup>[20]</sup> If the coefficient  $b$  is close to 1, the electrochemical reaction is highly influenced by the capacitive behavior, whereas if  $b$  is close to 0.5, the diffusion process is dominant. The values of  $b$  with 0.750, 0.780, 0.805, and 0.856 for NMO/LTCNTs cathodes reveal that the kinetics for the self-supporting cathode is largely dominated by the capacitive contribution. Meanwhile, the  $b$  values of NMO cathode are 0.608 and 0.701, which means the kinetic of the NMO cathode is closer to diffusion-controlled process. The existence of CNTs increases

the capacitive contribution in the cathode, which is in agreement with the previous literature.<sup>[21]</sup> Then, we patterned the relationship between the normalized capacity and the sweep rate ( $\nu$ ), as shown in Figure 3c,f. With the increase of scan rates, the normalized capacity of NMO cathodes has a more obvious decreasing trend than that of NMO/LTCNTs, which also shows a better high-rate performance of NMO/LTCNTs.

Ex situ XRD analysis was performed to investigate the energy-storage mechanism for the NMO/LTCNTs cathodes at the specific voltage, as shown in Figure 3i. The structural evolution of NMO/LTCNTs was investigated by ex situ XRD measured at specific states of charge and discharge processes from 0.8 to 1.9 V under the current density of  $2 \text{ A g}^{-1}$ , and the SEM images of the electrodes at the conditions of full discharge at 0.8 V and full charge at 1.9 V are shown in Figure S2a,b, Supporting Information. According to the XRD patterns shown in Figure 3g, there is no significant phase variation during the

charge and discharge processes. A  $1^\circ$  peak shift at the characteristic peak (002) was observed during the charge process and the peak gradually becomes inconspicuous during the discharge owing to the intercalation and deintercalation of  $\text{Zn}^{2+}$ , reducing the intensity of the characteristic peaks during cycling.<sup>[14,22]</sup> Similar as in other aqueous ZIBs,  $\text{Zn}_4\text{SO}_4(\text{OH})_6 \cdot 5\text{H}_2\text{O}$  (ZHS) is generated on the cathode during discharge.<sup>[23]</sup> However, as shown in Figure 3h, the peaks of the deposition disappear during the charge process, which reveals the reversible cation intercalations.<sup>[24]</sup> Specifically, during the discharge process, the current flows to the cathode, and the  $\text{H}^+$  and  $\text{Zn}^{2+}$  get the cathode, which is based on the dual-ion intercalation mechanism of aqueous ZIBs, resulting in the formation of ZHS on the cathode. When  $\text{H}^+$  and  $\text{Zn}^{2+}$  leave the cathode during the charging process, ZHS disappears.<sup>[25]</sup> The formation of ZHS can be expressed by Equation (2).

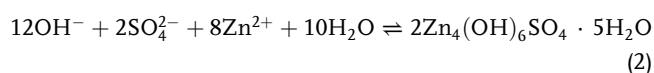
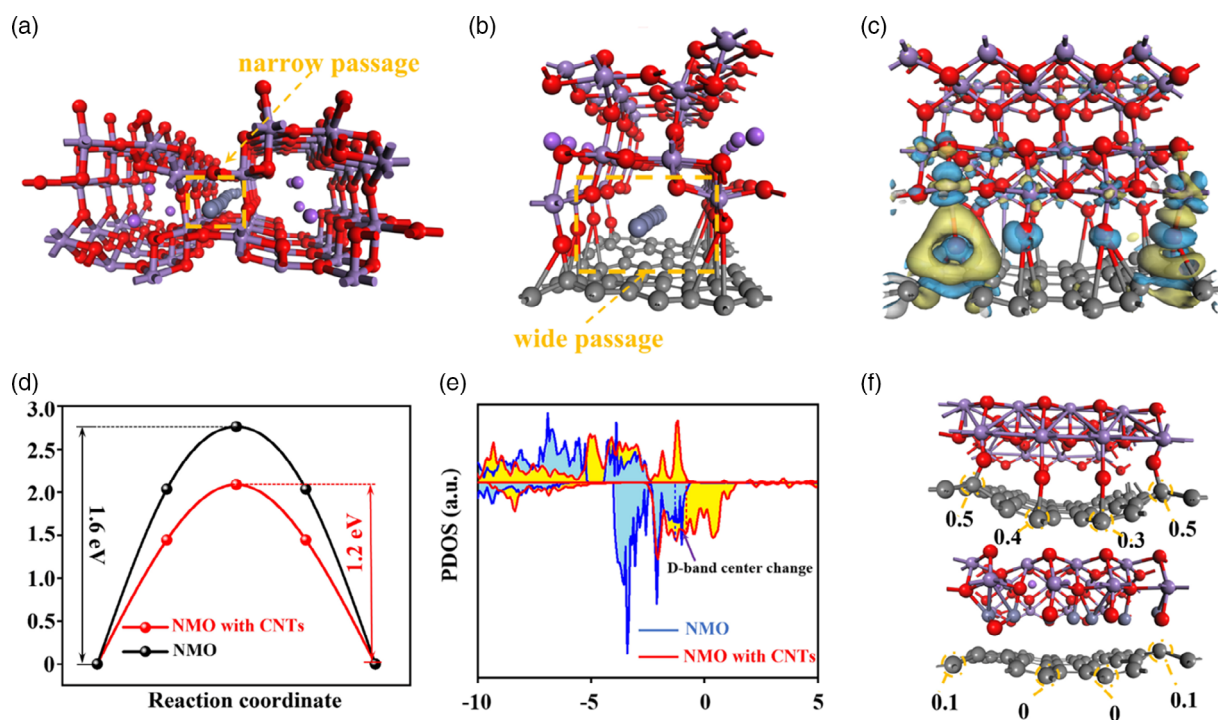


Figure 3h shows the discharge process from 1.9 to 0.8 V, and the amount of ZHS is increased on the cathode, which is also consistent with other literature.<sup>[26]</sup> As a typical  $\text{MnO}_2$ -based cathode, proton intercalation in NMO/VTCNTs cathode was also demonstrated in O 1s of ex situ XPS, as shown in Figure S2, Supporting Information. In addition to the generation of ZHS, the peak of Mn–OH was significantly enhanced in the initial cycle, which corresponds to the  $\text{H}^+$  intercalation/deintercalation of  $\text{MnO}_2$ -based cathode, as shown in Equation (3).



As the cycle progresses, due to the poor reversibility of ZHS, ZHS will be accumulated and covered on the surface of the cathode material after long-term cycling (50 cycles at a current density of  $0.2 \text{ A g}^{-1}$ ), resulting in the enhancement of the H–O–H peak signal in Figure S2, Supporting Information. Regardless of the initial cycle or long-term cycle, the intensity of Mn–O–Mn peak in the charge state is higher than that in the discharge state, which indicates that the reversible proton intercalation and deintercalation occurs throughout the cycle. The same phenomenon was also confirmed in Mn 2p of ex situ XPS in Figure S3, Supporting Information, but this difference in Mn signal intensity becomes smaller due to the accumulation of ZHS in long-term cycling. The generated ZHS presents a typical sheet-like structure covered on the cathode surface, as shown in Figure S4a, Supporting Information. However, due to the coverage of ZHS on the surface, the signal of Mn element is blocked, showing very little distribution on the surface, as shown in Figure S4f, Supporting Information.

DFT simulations were performed to reveal the mechanism inside the attracting behaviors how the interfacial structure efficiently enhances the battery performance. We compared the bulk NMO and NMO–CNT interlayer structures in terms of migration barriers and density of states, respectively. As presented in Figure 4a,  $\text{Zn}^{2+}$  can only migrate in narrow channels, which greatly reduces the migration rate of  $\text{Zn}^{2+}$ , posing a great hindrance to the long-cycling stability performance of batteries. Quite the opposite, a large space emerges in the interface of NMO–CNT, which allows  $\text{Zn}^{2+}$  to migrate more smoothly in



**Figure 4.** Schematic diagram of the migration of zinc ions in the a) bulk NMO and b) at the interface of NMO and CNT. c) The charge density difference at the interface. d) The migration barrier when  $\text{Zn}^{2+}$  transfers at the bulk NMO and interface of NMO and CNT. e) The projected density of states of Mn 3D-orbital at the bulk NMO and interface of NMO and CNT. f) The Bader charge change of C before and after Zn insertion.

the cathodes. The migration barrier of the  $\text{Zn}^{2+}$  in the bulk NMO (1.6 eV) and interface (1.2 eV) also provide numerical proof for the previous conclusions in Figure 4d. In addition, a large number of transferred electrons, observed in Figure 4c, indicate that the Mn–O–C bond greatly alters the chemical environment of the Mn ions.<sup>[27]</sup> To further understand the effect of this change on the battery performance, we analyzed the d orbitals of the Mn ions of bulk NMO and NMO at the interface. As presented in Figure 4e, the d orbitals of Mn are significantly altered. More orbitals at the Fermi energy level of the Mn ions near the interface make it easier for NMO–CNT to complete the electron transfer during the charging and discharging processes. In addition, we calculated the d-band centers of Mn ions in two different chemical environments. Our results demonstrated that the d-band center of Mn ion at the interface is closer to the Fermi energy level than that of bulk NMO. It indicates that the Mn ions at the interface are more active to gain or lose electrons to complete the electrochemical reaction, which effectively ensures the smoothness of the reaction. Also, to analyze the enhancement of the specific capacity of NMO–CNT compared to NMO, we performed a calculation of the Bader charge of C at the interface before and after embedding zinc ions. In Figure 4f, we can see that the Bader charges of C at the interface are 0.5, 0.4, 0.3, and 0.5 respectively, before embedding zinc ions. After embedding zinc ions, the Bader charge of C changes to 0.1, 0, 0, and 0.1, individually. This implies that carbon also gains electrons to undergo valence changes upon embedding zinc ions, suggesting that CNTs also contribute to the overall specific capacity, which is well corroborated with our experiments. The previous simulations indicate that interface structure can not only improve the ionic and electronic conductivity, but also contribute significantly to the specific capacity.

When only HTCNTs were applied to the fabrication for free-standing binder-free cathodes, even at low mass loading of  $\approx 1 \text{ mg cm}^{-2}$ , the ZIBs with NMO/HTCNTs cathodes exhibit a specific capacity of  $88 \text{ mAh g}^{-1}$  at a current density of  $2 \text{ A g}^{-1}$  after 1000 cycles (as shown in Figure S5, Supporting Information), which is comparable to typical electrochemical performance of NMO cathodes (with Super P and PVDF binders). Meanwhile, NMO/LTCNTs can exhibit excellent electrochemical performance ( $147 \text{ mAh g}^{-1}$  at  $2 \text{ A g}^{-1}$ ) under low mass loading conditions of  $\approx 1 \text{ mg cm}^{-2}$  (Figure S5, Supporting Information). However, when we fabricated NMO/LTCNTs to high mass loadings, their specific capacity was adversely affected. Although LTCNTs should have more surface than HTCNTs, the higher entanglement degree of LTCNTs can increase the potential barrier for electron migration.<sup>[28]</sup> Such adverse effect is amplified when increasing the mass loading, thus impairing the electron dynamics (as shown in Figure S6, Supporting Information). Therefore, the high mass loading NMO/VTCNTs self-supporting cathode was further subjected to electrochemical testing. Rate performance, which is significant for the practical application in the reality, is further tested in an increasing specific current range of  $0.1\text{--}5 \text{ A g}^{-1}$ . The rate testing profile of the ZIB with NMO/VTCNTs cathode is shown in Figure 5a, giving some basic information of the electrochemical reaction during the charge and discharge process. Stable voltage platforms are obviously visible in both charge and discharge process, indicating an active electrochemical property of the cathode material.<sup>[29]</sup> When the

current density is as low as  $0.1 \text{ A g}^{-1}$ , the charging voltage platforms are at 1.51 and 1.58 V. As the current density increases, the voltage platforms tend to rise slightly, which matches the charging process of CV curves in Figure 3a, showing a similar electrochemical property to those of NMO/LTCNTs. When the current density reaches  $5 \text{ A g}^{-1}$ , the two charging voltage platforms merge into one and reach 1.62 V. The discharging voltage platform of 1.32 V at  $0.1 \text{ mAh g}^{-1}$  is also found in Figure 3a. A slight downward shift of the voltage platforms during discharging process as current density increases also shows a good consistency with the CV curves. In the first 30 cycles of the rate testing, the ZIB with NMO/VTCNTs offers a high specific capacity of nearly  $400 \text{ mAh g}^{-1}$  under a current density of  $0.1 \text{ A g}^{-1}$ . When the current density increased from  $0.1$  to  $5 \text{ A g}^{-1}$  and back to  $0.1 \text{ A g}^{-1}$ , the prepared ZIB with NMO/VTCNTs cathode still shows a high capacity of  $357 \text{ mAh g}^{-1}$  (as shown in Figure 5b). When the current density rises to  $5 \text{ A g}^{-1}$ , the specific of NMO/VTCNTs cathode can maintain  $110 \text{ mAh g}^{-1}$ , which is nearly three times than that of NMO cathode, showing an extraordinary high-rate performance. This is reasonable because we found the better superiority of NMO/VTCNTs over NMO in high-rate testing in the previous CV curves. In addition, the NMO cathode without adding CNTs has a relatively longer activation process due to poor reaction kinetics.

One reason why the introduction of CNTs can greatly improve the electrochemical performance of NMO is to significantly reduce the polarization during battery charging and discharging. High polarization often brings sluggish transport kinetics, poor rate performance and low specific capacity.<sup>[30]</sup> As shown in Figure S7, Supporting Information, the electrochemical profile of initial reversible cycle of NMO/VTCNTs and NMO shows significantly smaller polarization of NMO/VTCNTs. For the free-standing binder-free cathode, in the initial reversible cycle, the polarization is about 167.1 mV, which is much smaller than the 465.0 mV of the NMO cathode on carbon paper. However, after the introduction of CNTs to form a 3D network, the enhancement of electrical conductivity and ionic conductivity provides excellent transport kinetics for battery cycling. In contrast, we believe that the interface formed by CNTs, especially LTCNTs, and NMO provides additional storage for ions. When LTCNTs and HTCNTs are respectively used as cathodes of ZIBs and cycled in the range of 0.8–1.9 V, they can only exhibit very limited specific capacities, as shown in Figure S8a,b, Supporting Information. Therefore, the improvement in charge storage brought by CNTs to NMO could be related to the interface they form. The decoupled transport of ions and electrons at the interface of ionic conductor and electronic conductor has been studied before, and the interface-dominated storage makes the motion of electrons and ions more likely to conform to 1D diffusion than conventional transport conditions within the space charge region.<sup>[31]</sup> Electron conduction occurs on CNTs and relies on the 1D hollow structure of CNTs, which is much faster than NMO as a semiconductor. Therefore, electron and ion transport mechanisms are theoretically faster in charge storage at the interface than in bulk charge storage. More importantly, based on the heterostructure of the NMO–CNTs interface and this decoupled transport of electrons and  $\text{Zn}^{2+}$  ions, the mobility of electrons and ions is improved, which is in line with the calculation results of lower energy barrier of  $\text{Zn}^{2+}$  transport in the

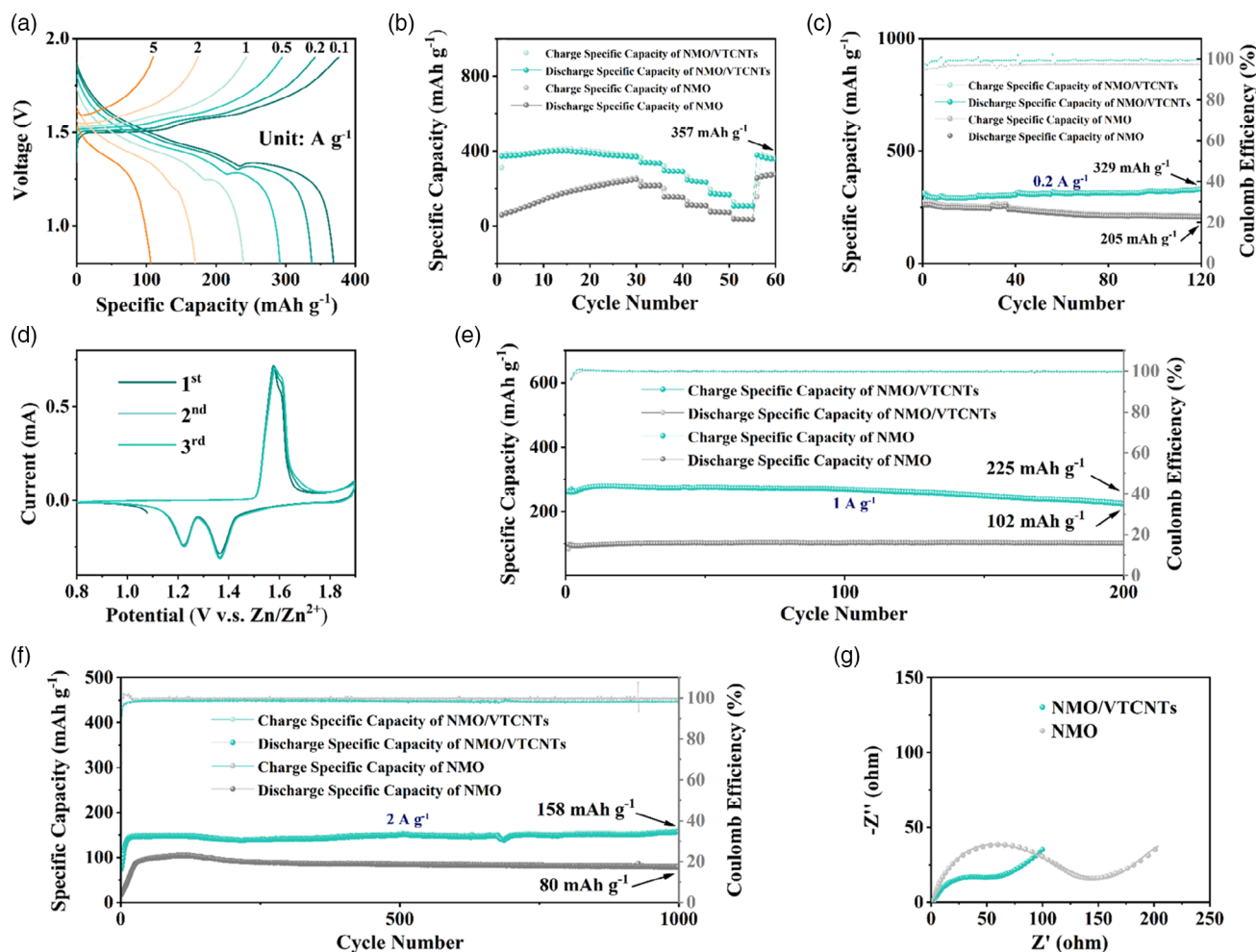


**Figure 5.** a) Galvanostatic charge and discharge profiles for NMO/VTCNTs full cell and b) cycle performance of NMO/VTCNTs compared with NMO at different current densities from 0.1 to 5 A g<sup>-1</sup>. c) Low-rate cycle performance of NMO/VTCNTs and NMO at a current density of 0.2 A g<sup>-1</sup>, which shows that the NMO/VTCNTs can exhibit a reversible specific capacity of 329 mAh g<sup>-1</sup> after 120 cycles. d) CV curves for the first three cycles of NMO/VTCNTs full cell. e) Cycle performance of NMO/VTCNTs and NMO at a current density of 1 A g<sup>-1</sup>, which shows that the NMO/VTCNTs can exhibit a reversible specific capacity of 225 mAh g<sup>-1</sup> after 200 cycles. f) Long-term cycle performance of NMO/VTCNTs and NMO at a current density of 2 A g<sup>-1</sup>, which shows that the NMO/VTCNTs exhibits a reversible specific capacity of 158 mAh g<sup>-1</sup> after 1000 cycles. g) Electrochemical impedance spectroscopy (EIS) test of NMO/VTCNTs and NMO full cells, showing a better conductivity of NMO/VTCNTs cathode.

interface in Figure 4d.<sup>[32]</sup> The following Equation (4) could be describe the zinc diffusion based on Fick's law.

$$j_{Zn} = -\frac{1}{F^2} \frac{\sigma_{ion}^{\alpha} \sigma_e^{\alpha}}{\sigma_{ion}^{\alpha} + \sigma_e^{\alpha}} \left[ \frac{\partial \mu_{ion}^{\alpha}}{\partial C_{ion}^{\alpha}} + \frac{\partial \mu_e^{\beta}}{\partial C_e^{\beta}} + F \frac{\partial (\varphi^{\alpha} - \varphi^{\beta})}{\partial C_M} \right] \quad (4)$$

$$\nabla C_M = -D^{\delta} \nabla C_M$$

Equation (4) describes the driving force of the diffusive flux, which is the gradient of the concentration. The value of  $\frac{\sigma_{ion}^{\alpha} \sigma_e^{\alpha}}{\sigma_{ion}^{\alpha} + \sigma_e^{\alpha}}$  can be higher in interface-dominated storage than in bulk storage because both  $\sigma_{ion}^{\alpha}$  and  $\sigma_e^{\alpha}$  are enhanced. The term  $F \frac{\partial (\varphi^{\alpha} - \varphi^{\beta})}{\partial C_M}$  is zero in bulk because of the homogeneity but nonzero in interfacial storage, causing the Zn<sup>2+</sup> diffusion coefficient ( $D_{Zn}$ ) to increase even more during interfacial storage.

To determine the cycling stability of the as-prepared materials, low-rate tests at a current density of 0.2 A g<sup>-1</sup> were carried out on NMO/VTCNTs and NMO, respectively. As shown in Figure 5c, the NMO/VTCNTs cathode with an active material mass loading of  $\approx 5 \text{ mg cm}^{-2}$  (total cathode mass loading of  $\approx 7.1 \text{ mg cm}^{-2}$ ) displays a discharge capacity of 329 mAh g<sup>-1</sup>, which is 1.60 times that of NMO cathode with an active material mass loading of  $\approx 1 \text{ mg cm}^{-2}$ . Meanwhile, the coulomb efficiency remains at  $\sim 100\%$  during the repeated charge and discharge cycles. It is found that the capacity of NMO/VTCNTs cathode increases slightly along the cycling, which is due to the gradual penetration of electrolyte into the spacing between the stacked CNTs. Figure 5d is the CV curves of the first three cycles of NMO/VTCNTs with a scan rate of 0.1 mV s<sup>-1</sup>, showing good reversibility and cycling stability, and further indicating its similar electrochemical behavior to NMO/LTCNTs by showing similar redox

peak position and intensity. As shown in Figure 5e,f, current densities of 1 and 2 A g<sup>-1</sup> were used to examine the high rate and long cycling performance of NMO/VTCNTs. At a current density of 1 A g<sup>-1</sup>, the ZIBs with NMO/VTCNTs cathodes can achieve a high specific capacity of 225 mAh g<sup>-1</sup> at 200 cycles, which is 2.21 times compared to that of NMO cathodes. When the current density is further increased to 2 A g<sup>-1</sup>, the NMO/VTCNTs cathode can still maintain a high reversible capacity of 158 mAh g<sup>-1</sup>, showing a retention rate of ≈100%. Electrochemical impedance spectroscopy (EIS) test of NMO/VTCNTs and NMO were carried out as shown in Figure 5g. The equivalent circuit fitting is shown in Figure S9, Supporting Information, respectively, showing the smaller ohmic resistance  $R_s = 1.85 \Omega$  and more efficient ion diffusion ( $R_{ct} = 60.61 \Omega$ ) of NMO/VTCNTs compared to NMO ( $R_s = 2.09 \Omega$  and  $R_{ct} = 558.18 \Omega$ ), representing an increase in conductivity. Given the slope of the low-frequency region of the Nyquist plot associated with the diffusion rate, the larger slope of NMO/VTCNTs (0.53) indicates a faster diffusion within the electrodes compared to NMO (0.44), as shown in Figure S10a,b, Supporting Information. The Table S1, Supporting Information shows the cathode electrochemical performance in ZIBs of manganese dioxide and its hybrid structures when combined with carbon materials, especially CNTs, reported in the past 2 years. It's worth noting that the prepared free-standing binder-free NMO/VTCNTs cathodes are exceptional when compared with the recent work under different current density conditions, which provides an important reference for the development of industrialization.

### 3. Conclusion

In this work, we report a strategy for the preparation of manganese-based free-standing binder-free cathodes with varying thinness CNTs to simultaneously increase the unit area mass loading of the active material and enhance the ionic and electronic conductivity of the electrode. Based on these advantages, the specific capacity of ZIBs made by prepared NMO with 3D varying thinness CNTs networks has been significantly increased. The resulting free-standing cathodes achieve excellent capacity performance (329 mAh g<sup>-1</sup> after 120 cycles at 0.2 A g<sup>-1</sup> and 225 mAh g<sup>-1</sup> after 200 cycles at 1 A g<sup>-1</sup>) and long-term cycling stability (158 mAh g<sup>-1</sup> at 2 A g<sup>-1</sup> after 1000 cycles) thanks to the benign composite of lamellar NMO with a network of CNTs. We not only report a ZIBs cathode composite nanomaterial with excellent electrochemical properties, but also propose a scalable strategy to utilize CNTs with different thinness to achieve high loading while maintaining high specific capacity. At the same time, the composite of CNTs with NMO provides a wider ion conduction channel at the interface based on density functional theory (DFT) calculations, which also provides an important reference for the study of nanocomposite interfaces.

### 4. Computation Methods

First principal calculations were carried out by the Vienna Ab initio simulation package (VASP) code. The cutoff energy was set as 550 eV, the  $\Gamma$ -centered  $k$ -mesh was set as  $3 \times 3 \times 3$  for all

calculations. The cell optimization was set as full to fully release the stress in the structure. The convergence for max force, stress, and displacement were 0.01 eV Å<sup>-1</sup>, 0.03 GPa, and 0.001 Å, individually. The Perdew–Burke–Ernzerh of generalized gradient approximation (GGA) and the ultrasoft pseudopotential for every atom were adopted.<sup>[33]</sup>

The crystalline structures are constructed from the crystalline structure database and experimental results. To explain the migration behavior of the Zn<sup>2+</sup> in the anode during the insertion process, we calculate the migration barrier when the Zn<sup>2+</sup> transfers at the bulk structure of NaMnO<sub>4</sub> and the NaMnO<sub>4</sub>–CNT interface. The complete linear synchronous transit (LST) and quadratic synchronous transit (QST) methods were employed to search the transition state (TS).<sup>[34]</sup> The nudged elastic band (NEB) method was applied to confirm the TS structure where the cutoff energy, the self-consistent field (SCT) convergence, max force, stress, and displacement are set as 550 eV,  $2.0 \times 10^{-5}$  eV atom<sup>-1</sup>, 0.02 eV Å<sup>-1</sup>, 0.1 GPa, and 0.002 Å, individually.<sup>[35]</sup>

The charge density difference is calculated based on Equation (5)

$$\Delta\rho = \rho_{\text{total}} - \rho_{\text{adsorbent}} - \rho_{\text{adsorbate}} \quad (5)$$

where  $\rho$  is the charge density of the corresponding structure.

## 5. Experimental Section

**Material Synthesis:** All chemicals were purchased from Sigma-Aldrich. NMO/LTCNTs was synthesized by a facile coprecipitation method, as shown in Figure 1a. All chemicals were purchased from Sigma-Aldrich without further purification. Solution A was prepared by dissolving 7.5 mmol of manganese (II) nitrate tetrahydrate in 10 mL of deionized water, solution B was prepared by 27.5 mmol of NaOH in 10 mL of deionized water, solution C was prepared with 5 mmol LTCNTs (small diameter of ≈5–10 nm) in 10 mL of deionized water, and solution D was a mixed solution of 6 mL of H<sub>2</sub>O<sub>2</sub> (30 wt%) and 45 mL of deionized water. Solution C was first sonicated for 20 min while solutions A and B were stirred for 10 min. Then, solution B and C were added to solution A quickly and stirred for an additional 5 min. After that, solution D was quickly poured into the mixture of solution A, B, and C with vigorous magnetic stirring for another 10 min. A black precipitate formed immediately in the solution, after which the solution was kept in an ice bath for 48 h to form solution E. After sufficient ageing, solution E was centrifuged at 4500 r min<sup>-1</sup> for 10 min and the resulting brown–black powder was freeze-dried for a further 48 h, at which point the NMO/LTCNTs hybrid nanomaterial was obtained. As a comparative sample, NMO was synthesized in the same way but without the involvement of CNTs.

The obtained NMO/LTCNTs were ground for 10 min and then mixed with HTCNTs in water in a ratio of 7:3 by mass and subjected to full sonication in an ultrasonic processor (UP400S, Scientific & Medical Products Ltd.) with a pause time of 0.5 s in the amplitude of 70% for 10 min. The final product was attached to the polyethersulfone membrane by suction filtration. After allowing it to dry naturally at room temperature, the electrode was peeled off to become a free-standing, binder-free cathode and achieved ≈ 5 mg cm<sup>-2</sup> of the active materials.

**Materials Characterization:** The change in crystal structure following poly(3,4-ethylenedioxythiophene) intercalation was investigated via XRD (Rigaku, miniFlex600) using Cu-K $\alpha$  radiation ( $\lambda = 0.70$  nm) in the range of 5°–40° (2 $\theta$ ) and Mo-K $\alpha$  radiation ( $\lambda = 0.15$  nm) in the range of 5°–70° (2 $\theta$ ). The morphologies of the samples were examined using a field-emission SEM (FE-SEM, FEI, Verios G4 UC) equipped with an EDS attachment. The samples were coated with platinum prior to SEM

analysis. For TEM (JEOL, JEM2100F), samples were dispersed in acetone and loaded onto a holey carbon grid for imaging. XPS was performed using a K-Alpha+ (Thermo Fisher Scientific Messtechnik) to observe the oxidative state at different voltages. Imaging Processing and Data Analysis: The micro-CT (ZEISS Xradia 620 Versa with 40x lens) projections were reconstructed using a filtered-back projection algorithm (XMReconstructor, Carl Zeiss Inc.). The reconstructed micro-CT datasets were imported into Avizo 2020.2 (ThermoFisher) for further segmentation and quantification. A median filter was applied to increase the signal-to-noise ratio. The pristine material, imaged by micro-CT, were segmented (based on gray scale values) into three phases consisting of active materials (NMO), CNTs, and pores.

**Electrochemical Measurement:** For non-free-standing, non-binder-free cathode materials, the slurry was prepared by mixing the active materials (NMO), carbon black (Super P, TIMCAL Graphite & Carbon), and poly(vinylidene fluoride) (PVDF, M.W. 534 000, Sigma-Aldrich) at a weight ratio of 7:2:1 using N-methyl-2-pyrrolidone (NMP); the mixture was then coated on carbon paper. After drying in a vacuum oven at 60 °C for 24 h, cathodes with  $\approx 0.45\text{--}1.5\text{ mg cm}^{-2}$  of the active materials were achieved. CR2032 coin cells were assembled by a traditional method in an open-air system using glass-fibers (Whatman, GF/A) and metallic Zn foils as separators and anodes, respectively. Additionally, 2 M ZnSO<sub>4</sub> and 0.2 M MnSO<sub>4</sub> was used as the electrolyte. The coin cells were tested using a WBCS 3000 automatic battery cycler (WonA Tech, Korea) at 25 °C. The current density and specific capacity were calculated using only the weight of the active material. CV tests were performed using a ZIVE SP1 potentiostat analyzer (WonA Tech, Korea) at 25 °C. CV tests were performed at various scan rates (0.8–1.9 V versus Zn<sup>2+</sup>/Zn). EIS tests were performed using a ZIVE SP1 impedance analyzer (WonA Tech, Korea) in the frequency range of 10<sup>5</sup>–10<sup>1</sup> Hz.

## Supporting Information

Supporting Information is available from the Wiley Online Library or from the author.

## Acknowledgements

X.G. thanks the funding support from China Scholarship Council/University College London for the Ph.D. scholarship. The authors would like to acknowledge the Engineering and Physical Sciences Research Council, United Kingdom (EPSRC, EP/L015862/1, EP/V027433/1).

## Conflict of Interest

The authors declare no conflict of interest.

## Data Availability Statement

The data that support the findings of this study are available from the corresponding author upon reasonable request.

## Keywords

carbon nanotubes, cathode structures, DFT calculations, Zn-ion batteries

Received: October 19, 2022

Revised: December 16, 2022

Published online:

- [1] a) Y. Liu, X. Lu, F. Lai, T. Liu, P. R. Shearing, I. P. Parkin, G. He, D. J. Brett, *Joule* **2021**, *5*, 2845. b) M. Zhou, Z. Bo, K. Ostrikov, *Phys. Chem. Chem. Phys.* **2022**, *24*, 20674; c) W. Zong, N. Chui,

- Z. Tian, Y. Li, C. Yang, D. Rao, W. Wang, J. Huang, J. Wang, F. Lai, *Adv. Sci. Lett.* **2021**, *8*, 2004142; d) H. Qin, W. Kuang, N. Hu, X. Zhong, D. Huang, F. Shen, Z. Wei, Y. Huang, J. Xu, H. He, *Adv. Funct. Mater.* **2022**, *32*, 2206695.
- [2] a) F. Wan, Z. Niu, *Angew. Chem. Int.* **2019**, *131*, 16508. b) H. Wu, G. Zheng, N. Liu, T. J. Carney, Y. Yang, Y. Cui, *Nano Lett.* **2012**, *12*, 904. c) J. Zhao, G. Zhou, K. Yan, J. Xie, Y. Li, L. Liao, Y. Jin, K. Liu, P.-C. Hsu, J. Wang, *Nat. Nanotechnol.* **2017**, *12*, 993; d) X. Gao, X. Sun, J. Liu, N. Gao, H. Li, *J. Energy Storage* **2019**, *25*, 100901.
- [3] a) M. Song, H. Tan, D. Chao, H. J. Fan, *Adv. Funct. Mater.* **2018**, *28*, 1802564. b) Y. Li, J. Zhao, Q. Hu, T. Hao, H. Cao, X. Huang, Y. Liu, Y. Zhang, D. Lin, Y. Tang, *Mater. Today Energy* **2022**, *29*, 101095; c) W. Kao-ian, A. A. Mohamad, W. R. Liu, R. Pornprasertsuk, S. Siwamogsatham, S. Kheawhom, *Batter. Supercaps* **2022**, *5*, 202100361.
- [4] K. Mensah-Darkwa, D. Nframah Ampong, E. Agyekum, F. M. de Souza, R. K. Gupta, *Energies* **2022**, *15*, 4052.
- [5] S. Gull, H.-Y. Chen, *MRS Energy Sustainable* **2022**, *9*, 248.
- [6] R. Zhang, P. Liang, H. Yang, H. Min, M. Niu, S. Jin, Y. Jiang, Z. Pan, J. Yan, X. Shen, *Chem. Eng. J.* **2022**, *433*, 133687.
- [7] S. Zhou, X. Wu, H. Du, Z. He, X. Wu, X. Wu, *J. Colloid Interface Sci.* **2022**, *607*, 1061.
- [8] a) Q. Xie, G. Cheng, T. Xue, L. Huang, S. Chen, Y. Sun, M. Sun, H. Wang, L. Yu, *Mater. Today Energy* **2022**, *24*, 100934; b) Y. Zuo, P. Liu, L. Ling, M. Tian, Z. Wang, H. Tian, T. Meng, X. Sun, S. Cai, *ACS Appl. Mater. Interfaces* **2022**, *14*, 26653; c) Z. Shang, H. Zhang, M. Wang, Q. Chen, K. Lu, *Nanoscale* **2022**, *14*, 6085.
- [9] Y. Zhang, S. Deng, M. Luo, G. Pan, Y. Zeng, X. Lu, C. Ai, Q. Liu, Q. Xiong, X. Wang, *Small* **2019**, *15*, 1905452.
- [10] Z. Wang, M. Zhang, W. Ma, J. Zhu, W. Song, *Small* **2021**, *17*, 2100219.
- [11] a) Y. Wang, F. Ye, Z. Wu, L. Jiang, L. Zhang, L. Hu, *ACS Appl. Energy Mater.* **2021**, *4*, 4138; b) W. Zong, H. Guo, Y. Ouyang, L. Mo, C. Zhou, G. Chao, J. Hofkens, Y. Xu, W. Wang, Y. E. Miao, *Adv. Funct. Mater.* **2022**, *32*, 2110016.
- [12] A. R. Mainar, E. Iruin, J. A. Blázquez, *Energy Technol.* **2020**, *8*, 2000476.
- [13] a) X. Gao, X. Sun, Z. Jiang, Q. Wang, N. Gao, H. Li, H. Zhang, K. Yu, C. Su, *New J. Chem.* **2019**, *43*, 3907; b) V. Petkov, *Mater. Today* **2008**, *11*, 28.
- [14] H. Dong, J. Li, S. Zhao, Y. Jiao, J. Chen, Y. Tan, D. J. Brett, G. He, I. P. Parkin, *ACS Appl. Mater. Interfaces* **2020**, *13*, 745.
- [15] a) S. Qiu, R. Guo, Q. Wang, F. Yang, Y. Han, X. Peng, H. Yuan, X. Wang, *Int. J. Energy Res.* **2021**, *45*, 14985; b) Y. Qiu, Z. Zhang, T. Zhang, P. Zhang, *Sci. Total Environ.* **2022**, *848*, 157802.
- [16] H. Qin, W. Kuang, D. Huang, X. Zhang, J. Liu, L. Yi, F. Shen, Z. Wei, Y. Huang, J. Xu, *J. Mater. Chem.* **2022**, *10*, 17440.
- [17] H. Tong, T. Li, J. Liu, D. Gong, J. Xiao, L. Shen, B. Ding, X. Zhang, *Energy Technol.* **2021**, *9*, 2000769.
- [18] H.-S. Wang, D.-Q. Huang, R.-M. Liu, *J. Electroanal. Chem.* **2004**, *570*, 83.
- [19] Q. Liu, A. A. Shinkle, Y. Li, C. W. Monroe, L. T. Thompson, A. E. Sleightholme, *Electrochem. Commun.* **2010**, *12*, 1634.
- [20] J. Li, K. McColl, X. Lu, S. Sathasivam, H. Dong, L. Kang, Z. Li, S. Zhao, A. G. Kafzas, R. Wang, *Adv. Mater. (Weinheim, Ger.)* **2020**, *10*, 2000058.
- [21] a) Y. Zhang, L. Wang, H. Xu, J. Cao, D. Chen, W. Han, *Adv. Funct. Mater.* **2020**, *30*, 1909372; b) S. Zeng, X. Zhou, B. Wang, Y. Feng, R. Xu, H. Zhang, S. Peng, Y. Yu, *J. Mater. Chem.* **2019**, *7*, 15774; c) Y. Ren, F. Meng, S. Zhang, B. Ping, H. Li, B. Yin, T. Ma, *Carbon Energy* **2022**, *4*, 446.
- [22] X. Liu, W. Ni, Y. Wang, Y. Liang, B. Wu, G. Xu, X. Wei, L. Yang, *Small* **2022**, *18*, 2105796.
- [23] a) P. Oberholzer, E. Tervoort, A. Bouzid, A. Pasquarello, D. Kundu, *ACS Appl. Mater. Interfaces* **2018**, *11*, 674; b) Y. Jiao, L. Kang, J. Berry-Gair, K. McColl, J. Li, H. Dong, H. Jiang,

- R. Wang, F. Cora, D. J. Brett, *J. Mater. Chem.* **2020**, *8*, 22075; c) X. Xu, Y. Chen, D. Zheng, P. Ruan, Y. Cai, X. Dai, X. Niu, C. Pei, W. Shi, W. Liu, *Small* **2021**, *17*, 2101901.
- [24] H. Chen, C. Dai, F. Xiao, Q. Yang, S. Cai, M. Xu, H. J. Fan, S. J. Bao, *Adv. Mater. Lett.* **2022**, *34*, 2109092.
- [25] T. Xue, H. J. Fan, *J. Energy Chem.* **2021**, *54*, 194.
- [26] Y. Wu, Y. Tao, X. Zhang, K. Zhang, S. Chen, Y. Liu, Y. Ding, M. Cai, X. Liu, S. Dai, *Sci. China Mater.* **2020**, *63*, 1196.
- [27] Y. Dai, X. Liao, R. Yu, J. Li, J. Li, S. Tan, P. He, Q. An, Q. Wei, L. Chen, X. Hong, K. Zhao, Y. Ren, J. Wu, Y. Zhao, L. Mai, *Adv. Mater.* **2021**, *33*, 2100359.
- [28] Z. Wu, K. Pei, L. Xing, X. Yu, W. You, R. Che, *Adv. Funct. Mater.* **2019**, *29*, 1901448.
- [29] G. Liang, F. Mo, D. Wang, X. Li, Z. Huang, H. Li, C. Zhi, *Energy Storage Mater.* **2020**, *25*, 86.
- [30] N. Zhang, M. Jia, Y. Dong, Y. Wang, J. Xu, Y. Liu, L. Jiao, F. Cheng, *Adv. Funct. Mater.* **2019**, *29*, 1807331.
- [31] C.-C. Chen, J. Maier, *Nat. Energy* **2018**, *3*, 102.
- [32] Y. Dai, X. Liao, R. Yu, J. Li, J. Li, S. Tan, P. He, Q. An, Q. Wei, L. Chen, *Adv. Mater. Lett.* **2021**, *33*, 2100359.
- [33] a) J. P. Perdew, K. Burke, M. Ernzerhof, *Phys. Rev. Lett.* **1996**, *77*, 3865; b) D. Vanderbilt, *Phys. Rev. B Condens. Matter.* **1990**, *41*, 7892.
- [34] a) T. A. Halgren, W. N. Lipscomb, *Chem. Phys. Lett.* **1977**, *49*, 225; b) G. Henkelman, H. Jónsson, *J. Chem. Phys.* **2000**, *113*, 9978.
- [35] G. Henkelman, B. P. Uberuaga, H. Jónsson, *J. Chem. Phys.* **2000**, *113*, 9901.